Article

Dynamics of the Magnetotail Plasma Sheet Current

Anthony Tat Yin Lui

The Johns Hopkins University Applied Physics Laboratory (JHU/APL), Laurel, MD 20723-6099, USA; tonylui1@hotmail.com

Abstract: Magnetospheric plasma can be investigated as a continuum by adopting magnetic field *B* and plasma flow *u* as primary parameters in the *Bu* paradigm or as a collection of individual particles by adopting electric field *E* and electrical current *j* as primary parameters in the *Ej* paradigm. It is pointed out that each paradigm has its merits and limitations. This viewpoint is illustrated further by examining several topics in magnetospheric research. The magnetic flux transport in substorm dipolarization is examined with the *Ej* paradigm to show why the *Bu* paradigm may be inappropriate in some cases due to the violation of the frozen-in condition for the validity of the *Bu* paradigm. There is no guarantee that large-scale plasma dynamics can always be treated accurately by the *Bu* paradigm. The disturbance revealed in the current disruption (CD) phenomenon has unique characteristics that can be more readily understood with the *Ej* paradigm. In a case study, the power dissipation in CD is evaluated to about an order of magnitude higher than that in the electron diffusion region associated with magnetic reconnection (MR). Two prominent plasma instabilities, namely tearing instability (TI) and cross-field current instability (CCI), are discussed and their relevance to substorm onset is evaluated. The mating instability developed conceptually is also briefly discussed. The development of azimuthal auroral beads (ABs) on auroral arcs formed prior to substorm onset is analyzed to show that CCI can predict well their wavelength, growth rate, and period simultaneously. In contrast, the observed azimuthal structures in ABs are inconsistent with TI that produces only meridian structures in the ionosphere. Overall, the physical insights gained in the *Ej* paradigm are helpful in achieving a deep understanding of several magnetospheric phenomena.

Keywords: Earth's magnetotail; current systems; current disruption; magnetic reconnection; magnetospheric substorm

1. Introduction

Plasma is the most abundant matter in the universe. The long-range force associated with its electric charge content has led to many behaviors quite distinct from other forms of matter. It is convenient to treat it as a continuous medium. The prevalence of this viewpoint has led to some researchers adopting its embedded magnetic field *B* and its bulk flow *u* as the primary parameters in the treatment of magnetospheric dynamics. This approach is called the *Bu* paradigm [1], which is based on the use of ideal magnetohydrodynamics (MHD) and is expected to be invalid when the frozen-in field is not satisfied. On the other hand, there are phenomena that are difficult, if not impossible, to reconcile with the *Bu* paradigm. A different paradigm adopting its embedded electric field *E* and its current density *j* as the governing parameters is called the *Ej* paradigm [2–6]. Both paradigms have their pros and cons.

The existence of dualism to treat plasma dynamics is not unique. For example, electromagnetic waves can be treated well by Maxwell's equation in many circumstances. However, the photoelectric effect cannot be understood without adopting the photon as a primary quantum entity for such an effect. In the past, there have been some debates on which paradigm is superior to the other, initiated by the *Bu* paradigm researchers insisting that it is the only correct approach [7–9]. However, these arguments have been addressed by the *Ej* paradigm [10,11] with the conclusion that which paradigm is better is

highly dependent on the magnetospheric phenomenon under investigation. Insisting on one paradigm being superior to the other to treat all magnetospheric problems would be inappropriate for scientific pursuits.

In this article, magnetotail phenomena and instabilities associated with the electric current nature of the magnetotail plasma sheet are discussed to highlight distinct advantages in understanding these activities from the *Ej* paradigm. As a background to this paradigm, a schematic diagram of the Earth's magnetotail is illustrated in Figure 1 where the primary electric currents are labelled. They are the cross-tail current, the ring current, and the field-aligned current. The cross-tail current flows from the dawn side of the magnetotail to the dusk side. The ring current encircles the Earth. The field-aligned current links the magnetotail current to the ionosphere.
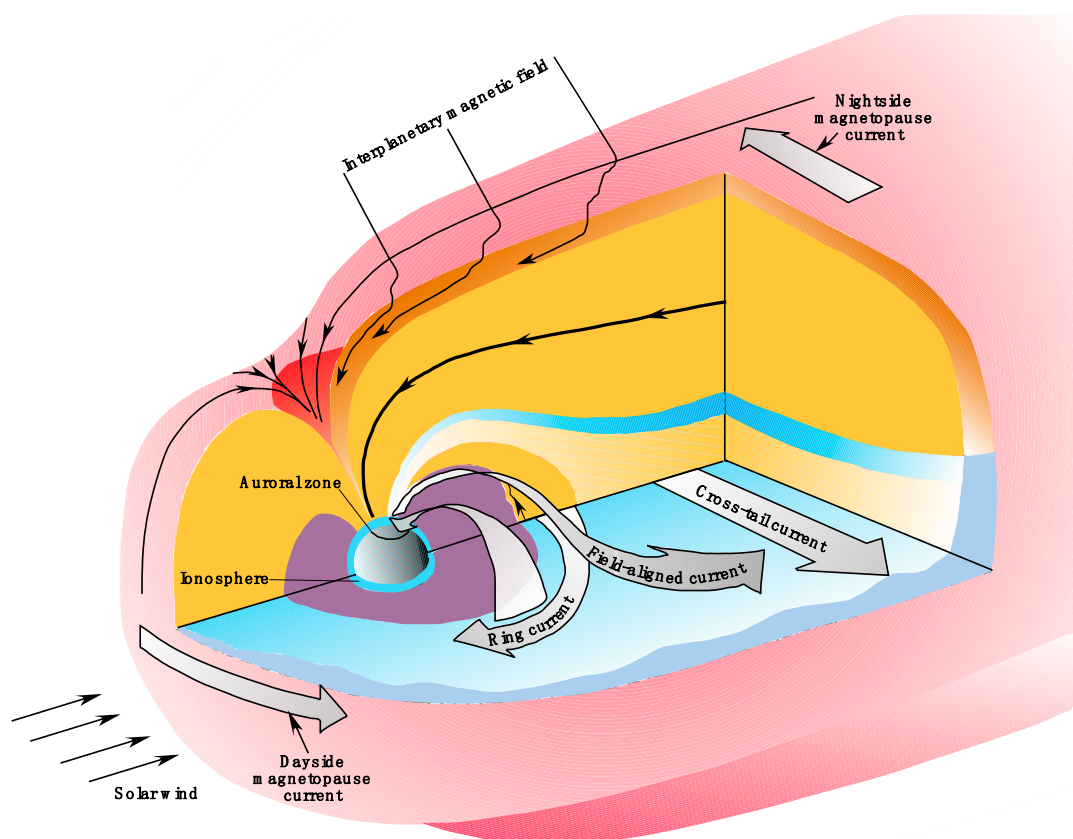

Figure 1. A schematic diagram to illustrate the primary current systems in the Earth's magnetotail plasma sheet.

The topics covered here include (1) the magnetic flux transport in substorm dipolarization, (2) the basic properties of current disruption phenomenon and its high level of power dissipation, (3) two prominent plasma instabilities that are often considered for current sheet disturbances in the magnetotail, and (4) formation of azimuthal auroral beads (ABs) on pre-substorm-onset auroral arcs and predictions of their characteristics (wavelength, growth rate, and period). In topic (1), the effectiveness in magnetic flux transport using the *Ej* paradigm will be evaluated to show why the *Bu* paradigm is not appropriate to address magnetic flux transport in some cases. In topic (2), current disruption (CD) properties are illustrated to show its departure from the *Bu* paradigm. The power dissipation in CD is estimated and compared with that in the electron diffusion region for magnetic reconnection (MR). In topic (3), two prominent plasma instabilities, tearing instability (TI) and cross-field current instability (CCI), in the magnetotail are discussed to reveal their characteristics, and in topic (4) kinetic features in ABs formation in pre-substorm-onset activities are used to show the predictions from CCI in reproducing the basic features of these ABs that are not compatible with TI.

2. Materials and Methods

Materials used are based on measurements from spacecraft in the Earth's magnetotail as well as ground-based stations that monitor space disturbances. The methods used are based on the well-known Newtonian mechanics equations and Maxwell's equations. For example, the integral form of the Ampere's law is used to infer the current density embedded in a layer bordered by two satellites separated only in the *z*-direction, with one above the layer and the other below the layer [12]. The embedded current density J_i ($i = x, y$) is given by

$$\mu_o J_i = \int \boldsymbol{B}_{\text{obs}}(z) \bullet d\boldsymbol{l}, \tag{1}$$

where μ_o is the permeability of free space, $\boldsymbol{B}_{\text{obs}}$ is the observed magnetic field, and the line integral is calculated on a rectangular loop. For $i = y$, the loop lies on the *XZ* plane with the short segments in the *x*-direction and the long segments in the *z*-direction to join the two satellites. Similarly for $i = x$, the loop lies on the *YZ* plane with the short segments in the *y*-direction and the long segments in the *z*-direction.

The magnitude of field-aligned current in the ionosphere $J_{||,i}$ is given by [13–15]

$$\mu_o J_{||,i} = B_i \int_{eq}^{ion} \left[\frac{2J_\perp \bullet \nabla B}{B^2} + \frac{\rho_m}{B} \frac{d}{dt} \left(\frac{\Omega_v}{B} \right) - \frac{J_{in} \bullet \nabla \rho_m}{\rho_m B} \right] dl_{||}, \tag{2}$$

where B_i is the magnetic field in the ionosphere, ρ_m is the mass density, $J_\perp$ is the perpendicular current density in the magnetosphere, and Ω_v is plasma flow vorticity. It is estimated in that, for the magnetotail plasma sheet, the second and third terms in Equation (2) are small in comparison with the first term.

The generalized Ohm's law is used to examine the transport of magnetic flux:

$$\boldsymbol{E} + \boldsymbol{U} \times \boldsymbol{B} = \frac{1}{\varepsilon_0 \omega_{pe}^2} \frac{d\boldsymbol{J}}{dt} + \frac{\boldsymbol{J} \times \boldsymbol{B}}{ne} - \frac{\nabla \bullet P_e}{ne} - \frac{1}{n}[\langle \delta \boldsymbol{E} \delta n \rangle + \langle \delta(n\boldsymbol{U}_e \times \delta \boldsymbol{B}) \rangle], \tag{3}$$

where $\boldsymbol{U}$ and $\boldsymbol{U}_e$ are the plasma and electron bulk flows, respectively, ε_0 is the permittivity of free space, ω_{pe} is the electron plasma frequency, n is the number density, P_e is the electron dynamic pressure tensor, $\langle \delta \boldsymbol{E} \delta n \rangle$ is the ensemble average of the product of $\boldsymbol{E}$ and n fluctuations, and $\langle \delta(n\boldsymbol{U}_e \times \delta \boldsymbol{B}) \rangle$ is the ensemble average of the cross product of $n\boldsymbol{U}_e$ and $\boldsymbol{B}$ fluctuations. If $\boldsymbol{E} = -\boldsymbol{U} \times \boldsymbol{B}$, magnetic flux is frozen-in with the fluid motion. This is called the frozen-in condition (FIC), and magnetic flux can then be visualized as being transported by the plasma flow $\boldsymbol{U}$.

A method used in wave analysis is to examine the temporal development of the wave from the wave dispersion relation. The momentum equation is used to evaluate the temporal behavior of electric and magnetic fields of the wave with their dependence on time as $e^{i\omega t}$, where ω is a complex quantity. If the imaginary part is positive, the wave will grow exponentially, and an instability will develop.

3. Results and Discussion

3.1. Magnetic Flux Transport

A magnetospheric substorm is a major space disturbance that poses several unanswered questions [16,17]. An important feature is the reconfiguration of the magnetic field in the magnetosphere at substorm onset. Prior to its onset, the magnetic field in the near-Earth magnetosphere is stretched considerably along its tail axis. At the onset, the near-Earth magnetic field is relaxed to become stronger and dipole-like. This reconfiguration, often referred to as dipolarization, requires prominent changes in the magnetic field content in the near-Earth region. In the **Bu** paradigm, such a change can only be made by transporting magnetic flux from one region to another. The procedure relies on verifying the FIC to be valid so that the plasma flow can be used to accomplish the transport. Such an essential assumption in addressing dipolarization during a substorm can be evaluated in the **Ej** paradigm by explicitly calculating the agreement between the two quantities $\boldsymbol{E}$ and $-\boldsymbol{U} \times \boldsymbol{B}$ for all three

components. If the equality is not valid for any one component, the FIC is invalid and magnetic flux cannot be considered as being transported by the plasma flow.

Magnetic structures from Earthward reconnection flows have been observed to show transient large northward swings in the magnetic field called dipolarization fronts (DFs), and [18–26]. Refs. [27,28] referred to the magnetic flux transport with DFs as dipolarizing flux bundles (DFBs). Ref. [29] reported a multi-case study of 18 cases of DFBs, and an evaluation of the FIC of these events with the generalized Ohm's law has been made [30].

Figure 2 shows a DFB on 27 February 2009. The 3 s spin-averaged B_z component in GSM coordinates for the four spacecrafts P1, P2, P3, and P4 is shown in the first column. The error bars are calculated based on the standard deviation of the mean (SDM) of the spin-averaged values from measurements at a higher resolution of 0.25 s. The U_x component in GSM coordinates based on the combined measurements from ESA and SST is shown in the second column. The comparison between the measured 3 s spin-averaged E_y component in the *dsl* coordinates (*dsl* is the despun satellite coordinates and is close to GSE coordinates) and the value of the $-(U \times B)_y$ component using U and B in the *dsl* coordinates is shown in the third column. The use of the *dsl* coordinates is better than GSE or GSM coordinates because the electric field is measured at this coordinate system and is therefore a more accurate way to compare the two quantities for the validity of FIC. Only the *y*-component is examined here because it is usually the largest component of these quantities. The error bars on E_y are derived from the SDM of the spin-averaged values based on measurements at a higher resolution of 0.125 s. The error bars on the $-(U \times B)_y$ component are based on the SDM of the magnetic field since no uncertainties are provided for U at the fast time resolution.

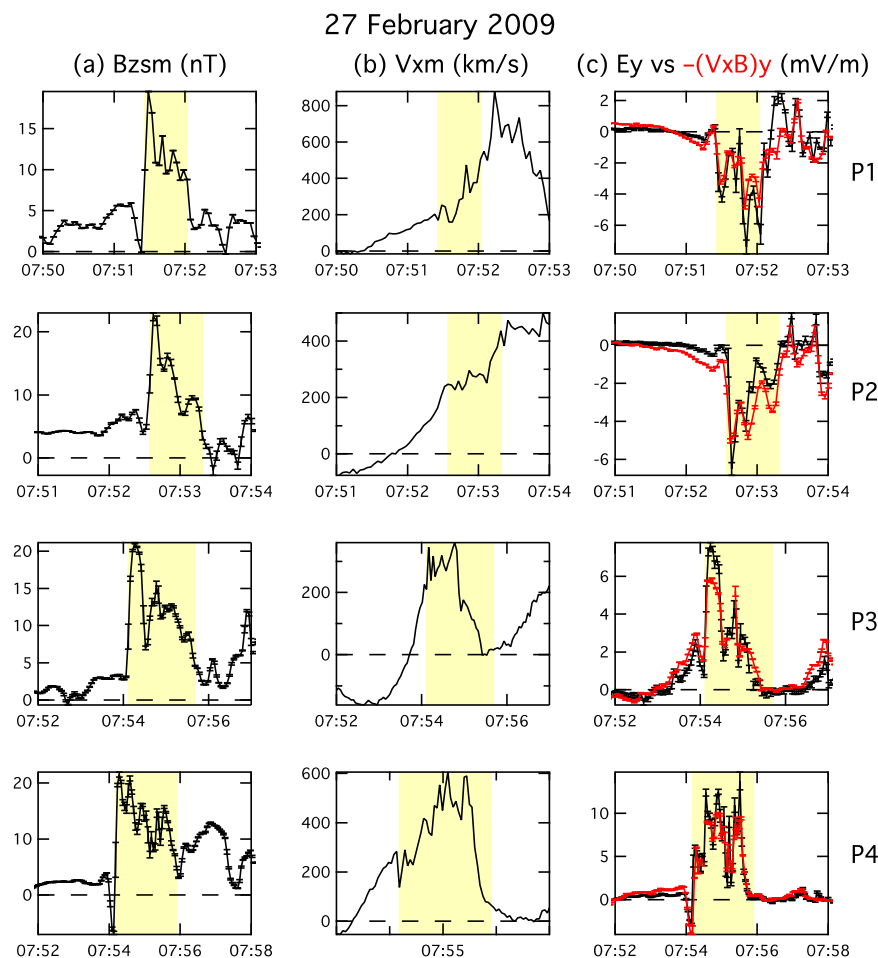**Figure 2.** The B_z component, plasma bulk flow Uxm, and comparison between E_y and $-(U \times B)_y$ for four THEMIS (Time History of Events and Macroscale Interactions during Substorms) satellites on 27 February 2009. The two quantities in evaluating the FIC agree reasonably well.

The DFB interval is highlighted in the figure. Prior to the arrival of DFB, the B_z component was quite small. A magnetic dip for ~1–2 min appeared at the front of the DFB ahead of sharp enhancement of the B_z component. Two of the dips had negative values. Earthward flows increased significantly in DFB. The comparison between the two frozen-in parameters shows generally good agreement; therefore, magnetic flux can be considered to be transported by plasma flow in this event.

Another example of DFB on 5 March 2009 is shown in Figure 3, which exhibits significant differences between the two quantities in FIC evaluation. In this event, there were substantial differences in the B_z component (from ~3 to ~10 nT), including its peak values (from ~12 to ~30 nT), within the DFB intervals among the four satellites. The magnetic dips ahead of the DFB were relatively small and did not become negative. Earthward flows were seen within the DFB for all satellites. Some significant tailward flows also occurred right after the DFB in P5 and P4.
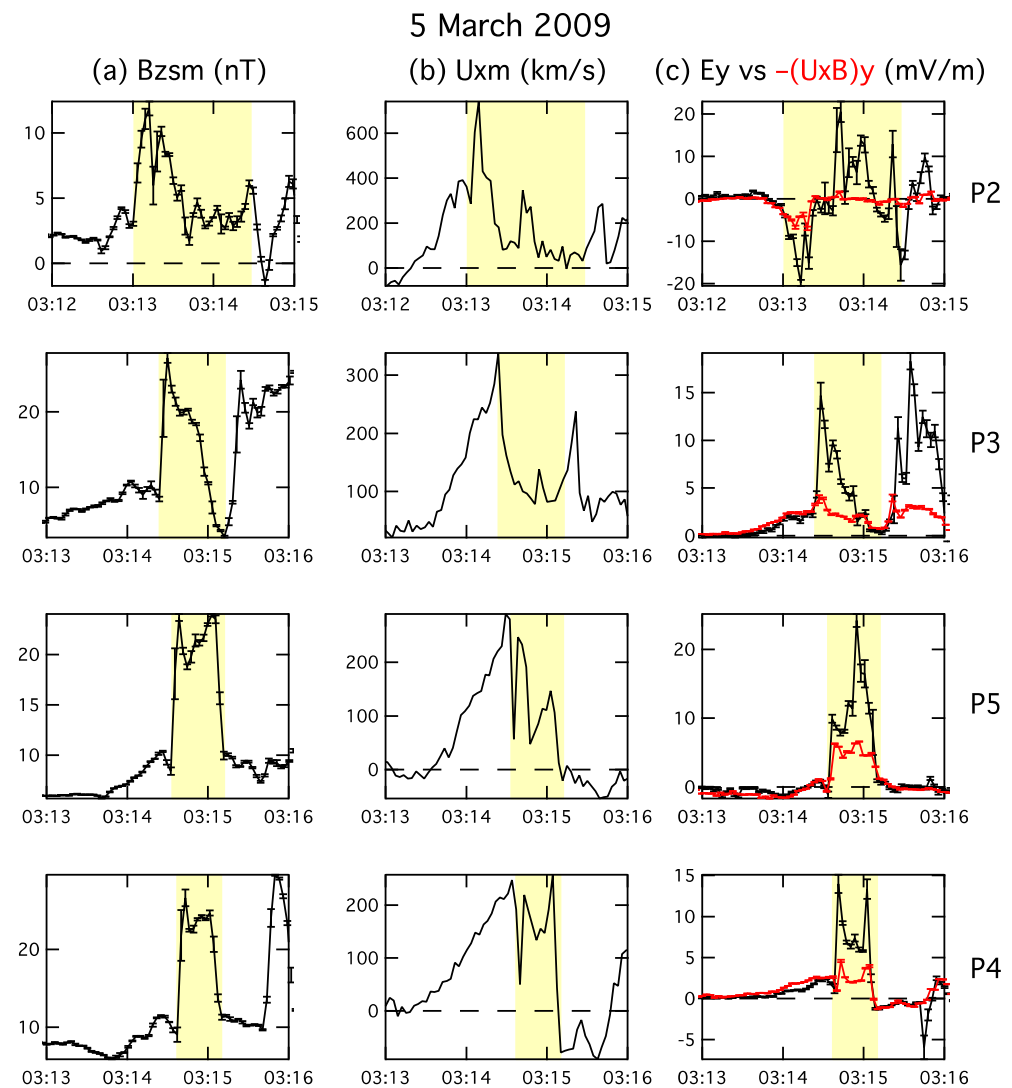

Figure 3. The B_z component, plasma bulk flow Uxm, and comparison between E_y and $-(\boldsymbol{U} \times \boldsymbol{B})_y$ for four THEMIS satellites on 5 March 2009. The two quantities in evaluating the FIC have significant differences.

The difference between the two FIC parameters can be quantified by comparing the magnitude of E_y and $-(\boldsymbol{U} \times \boldsymbol{B})_y$. This comparison ($= |E_y/(\boldsymbol{U} \times \boldsymbol{B})_y|$) is called the comparison ratio (CR). In calculating CR, it is limited to intervals when the electric field exceeds 0.5 mV/m to eliminate times of low-level electric fluctuations. Two criteria can be set up. For a lenient criterion, the FIC is invalid when CR is more than two because the

two FIC parameters differ by more than a factor of two. A stricter criterion can be used to describe the situation when the magnitude of E_y differs from the magnitude of $(U \times B)_y$ by 50%. In this event, CR is 0.7–10.6, 1.6–3.0, 0.9–2.6, and 0.7–2.5 for P2, P3, P5, and P4, respectively, demonstrating that the magnetic flux cannot be considered as being carried by the plasma flow with either criterion. An examination of all 18 cases reported by [29] shows that 9 of them did not satisfy the FIC under the lenient criterion. For the stricter criterion, as much as 94% of DFB do not satisfy the FIC. Therefore, the **Bu** paradigm is highly inaccurate for magnetic flux transport consideration.

It is estimated that the amount of transported magnetic flux needed in the near-Earth region for a substorm is ~0.5–1 GWb [31]. An individual DFB can transport an accumulated magnetic flux of ~0.1–2.2% of the requirement, indicating that it would require a minimum of ~50 DFBs for the amount needed in a substorm interval [30]. A similar conclusion is reached by [32]. Substorm dipolarization from magnetic flux transport belongs to large-scale plasma dynamics in the magnetosphere. Therefore, contrary to the expectation expressed in [9], there is no guarantee that large-scale plasma dynamics can always be treated accurately by the **Bu** paradigm.

3.2. Current Disruption

A rather unexpected behavior of the near-Earth magnetic field was discovered by [33] with the spacecraft Charge Composition Explorer (CCE). The satellite was at ~9 R_E in the midnight sector of the magnetotail. The onset of the high-level magnetic field fluctuations, which is a marked signature of CD and shown in Figure 4, was preceded by ~1 min onset by Pi2 pulsation at Kakioka station. The occurrence of Pi2 pulsation is a typical indicator of a substorm onset.
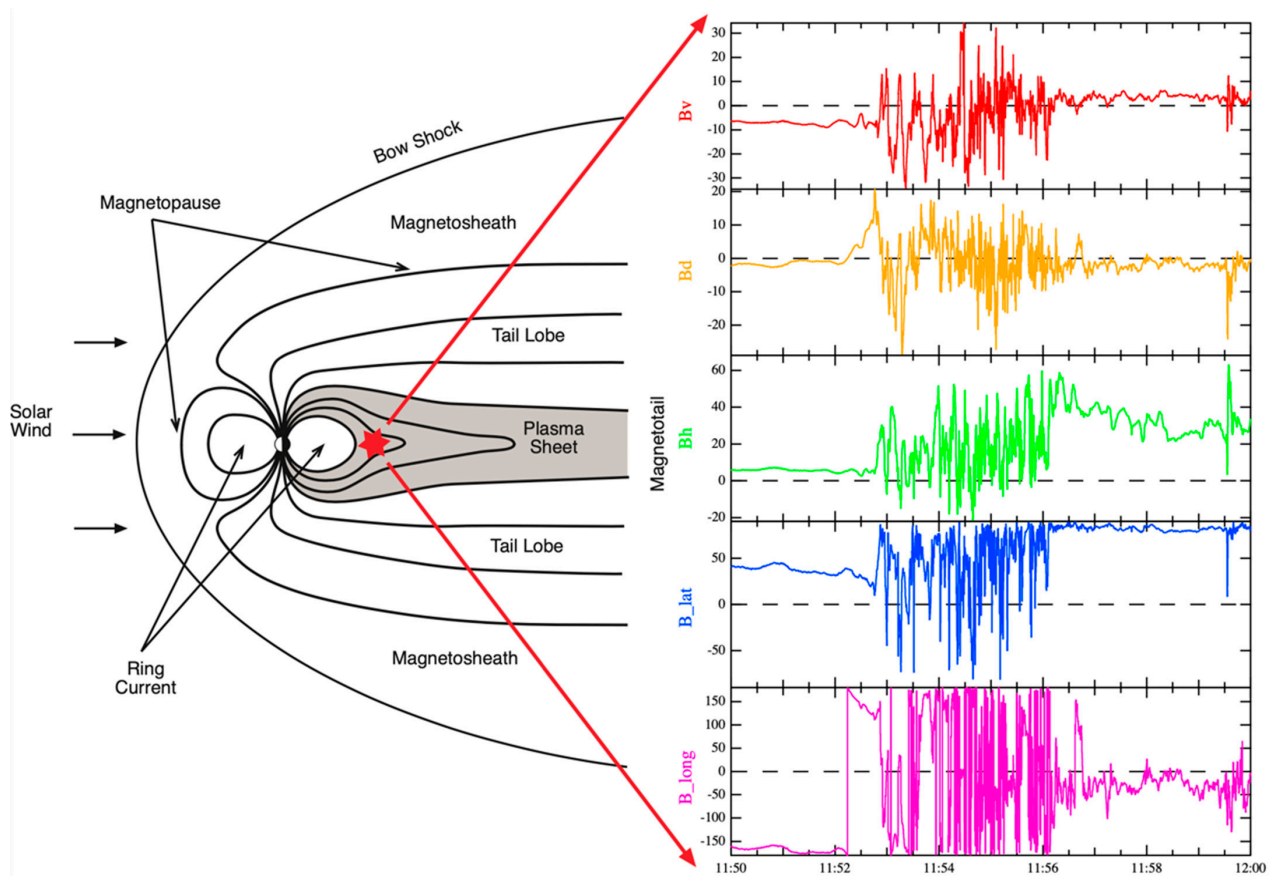

Figure 4. A case of CD is shown to indicate its proximity to Earth in the usually dipolar region (**left**); the measured rapid fluctuations of the magnetic field components at the site (**right**). The components of the magnetic field: Bv is the vertical component; Bd is the declination component; Bh is the horizontal component; B_lat is the latitude angle; and B_long is the longitudinal angle.

A more complete description of CD is as follows. The CD phenomenon has been identified by large magnetic fluctuations predominantly around the central plasma sheet where $B_z \gg B_x, B_y$. The B_z fluctuations can reach a level such that $\delta B_z / B_{zo}$ (B_{zo} is the B_z value before CD onset) is of the order one or larger. It typically lasts for several minutes, and B_z may become negative to overcome even a strong initial background magnetic field component. CD is accompanied by particle energization from the associated intense electric field. The local current becomes filamentary and may reverse its direction. A distinct feature of CD, unlike MR, is that the associated plasma flow pattern is not governed by the B_z polarity. The FIC is often not satisfied. Furthermore, the B_z component is significantly enhanced after CD with the relaxation of a stretched magnetic field to a more dipolar appearance. Several features of CD are illustrated in Figure 5.
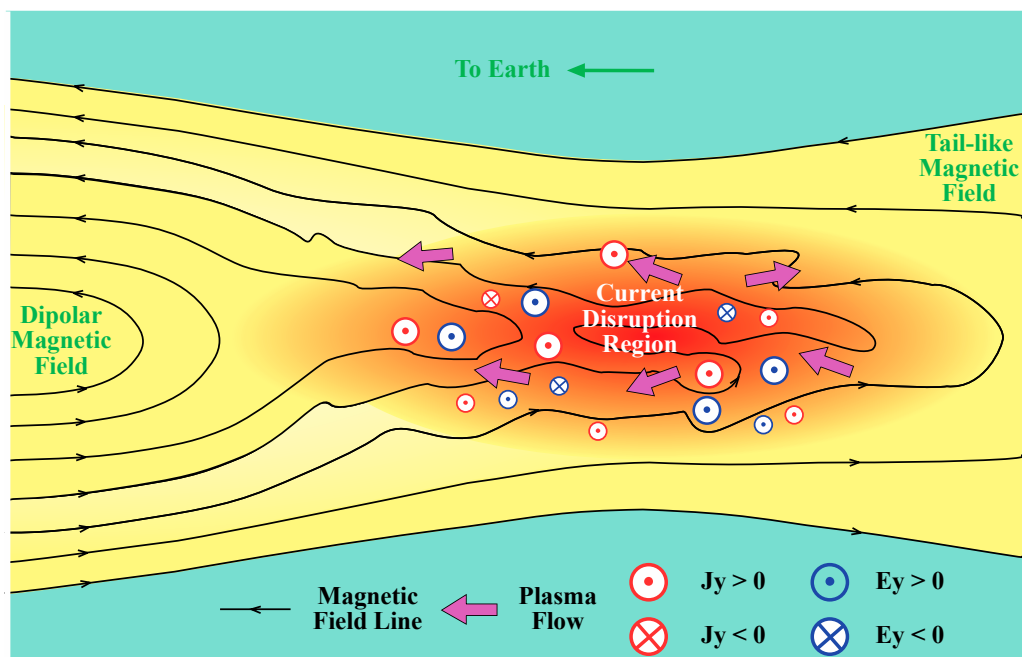

Figure 5. A schematic diagram to illustrate several features of CD. The sense of the y-component of the cross-tail current and the y-component of the electric field is indicated by the sign of **Jy** and **Ey**, respectively. The current and electric field can reverse their sign locally. The CD occurs in a closed magnetic field region unconnected to MR.

The CD activities are unrelated to MR. It has been shown in a detailed case study that the CD activity site approached the satellite from the Earthward side, as revealed by the remote sensing capability from the ion sounding technique [34]. If it were related to MR, the B_z component would be negative tailward of the MR site. However, observation indicated that the B_z component was strongly positive, contrary to the anticipated behavior of the B_z component pattern tailward of an MR site.

The basic structures in CD have never been produced by global simulations using the fluid equations in the ***Bu*** paradigm. However, particle-in-cell (PIC) simulations in the ***Ej*** paradigm have been reported to produce these structures [35,36]. The physical process for the disturbance is attributed to cross-field current instability by [35] and to ballooning/interchange instability by [36].

How current density changes during CD is demonstrated well by observations on 28 February 2009 when two of the THEMIS satellites were almost at an identical location on the *XY* plane but were separated by ~0.6 R_E in the *z*-location. This fortuitous situation occurred at the start of a magnetospheric substorm as indicated by the auroral indices at the top panel of Figure 6. The magnetic field components at P4 and P5 were given by the second and third panels, respectively. The current densities $J_{x,y}$ embedded within P4 and P5 are calculated based on the formula Equation (1) in Section 2.
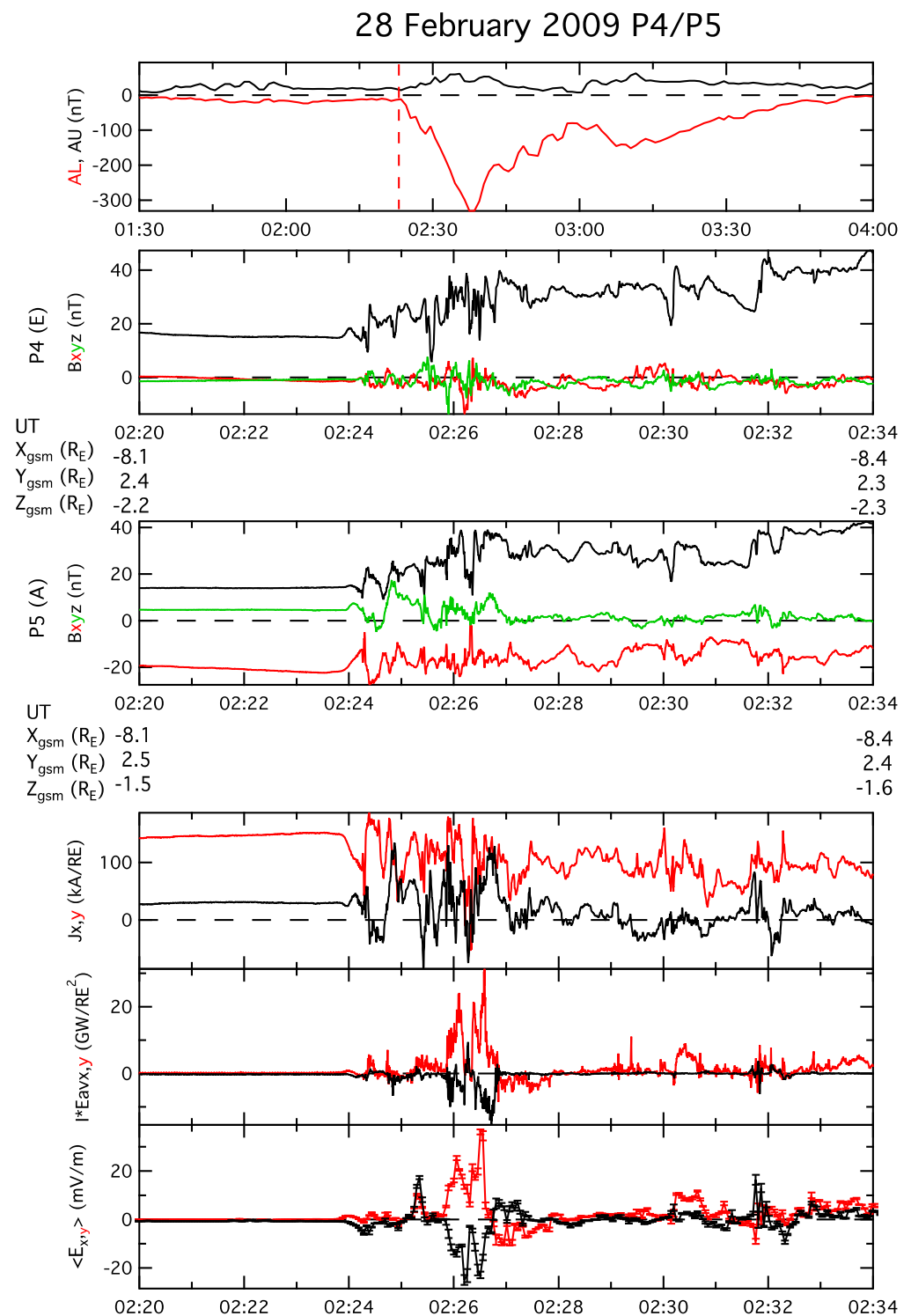
Figure 6. Observations of CD on 28 February 2009 showing the AU/AL (auroral upper/auroral lower) indices, the magnetic field components in GSM coordinates at P4 and P5, current densities in the layer embedded by P4 and P5, power within the layer, and the average electric field at the two satellites at CD.

The second last panel of Figure 6 shows the dissipation parameters in both *x*- and *y*-directions using different colors. The last panel shows the average electric field of the two satellites, also in both *x*- and *y*-directions using different colors. Note that since the power dissipation is mainly caused by the electric field, the role of CCI in power dissipation during a substorm is the rapid magnetic field changes as a result of current changes caused by the CCI.

There was a slight increase in J_y from 100 to 107 kA/R_E and a slight decrease in J_x from 31 to 25 kA/R_E just before CD onset. At CD onset, a sharp drop in J_y (from 107 to 63 kA/R_E) occurred, accompanied by a substantial increase in J_x (from 25 to 42 kA/R_E). These changes suggest a part of J_y was directed Earthward initially. There were large fluctuations in both J_x and J_y with occasional magnitudes larger than their initial magnitudes, which is interpreted as turbulence occurring in CD with current filamentation and transient local changes. The value of J_x even became negative at several short intervals. At the end of the interval, J_y and J_x settled down to 63 and 11 kA/R_E, respectively; these changes represent a reduction of 41% and 56% in J_y and J_x, respectively.

One may make an estimate to the overall power dissipation in CD. The average value of dissipation during the time interval from 2:24:20 to 2:26:50 is 4.38 GW/R_E^2. Choosing the *z*-dimension of CD to be the *z*-separation of P4 and P5 (~0.6 R_E), the *x*-dimension of CD is the ion gyroradius instead of the convective length of the structure. For the CD interval (02:24:18 to 02:26:17 UT), the ion gyroradius is ~391 km ~0.061 R_E with the average B_z of 20.4 nT and average ion temperature of 6.1 keV. The total power dissipation is ~31 W/m in the *y*-direction. This dissipation can be compared with that of the electron diffusion region detected by MMS-3 [37], which is 0.2–0.3 nW/m^3. Its *x*- and *z*-dimensions in units of electron Debye length d_e are 12–17 d_e (350–500 km) and 1–2 d_e (30–60 km), respectively. The *xz*-area is 1.1–3.0 m^2, leading to a total dissipation of 2.1 W/m in the *y*-direction, which is about one order of magnitude smaller than that in CD. This result is primarily due to the small dimensions of the electron diffusion region, but MR can be assumed to exist for a long time since it is not clear when MR may be terminated. On the other hand, CD only lasts for a few minutes and by itself cannot be compared with the substorm duration. However, multiple CDs such as in an avalanche system are envisioned to occur during a substorm interval [10,38,39]. Therefore, these two processes may yield comparable total dissipation during a substorm.

3.3. Plasma Instabilities

There are several plasma instabilities proposed for the onset of substorms that are related to the magnetotail plasma sheet. They are tearing instability, cross-field current instability, lower-hybrid drift instability, drift kink/sausage instability, current-driven Alfvénic instability, Kelvin–Helmholtz instability, and entropy anti-diffusion instability. A review of these instabilities has been documented in [35]. Here, only two prominent instabilities that had been updated since then are discussed below.

For simplicity, multiscale current sheets are not considered here. There are several nonlinear dynamics processes involved in a multiscale current sheet that can give rise to a significant destruction of its equilibrium, although they are not classified as plasma instabilities, e.g., "aging" of magnetotail thin current sheet [40] and offset of marginal stability by electron pressure anisotropy [41]. There are also other current sheet equilibria that may lead to its drastic changes, such as a super-thin current sheet [42] and equilibrium offset from a mixture of regular and chaotic charged particle motions [43]. Some of these processes are recently discussed in some details in [44].

3.3.1. Tearing Instability

This instability was first proposed by [45]. With the adoption of a Harris current sheet, the growth rate γ is found to be

$$\gamma = \pi^{1/2}(u_e/L)(\rho_e/L)^{3/2}(1 + T_i/T_e)(1 - k_x^2 L^2), \quad (4)$$

where u_e is the electron thermal speed, ρ_e is the electron gyroradius, T_i and T_e are the ion and electron temperatures, L is the half-thickness of the Harris current sheet, and k_x is the wavenumber of the tearing mode in the *x*-direction. Even for an extremely long wavelength mode with $k_x^2 L^2 \gg 1$, the growth rate is extremely slow with an *e*-folding time of ~1 h,

unsuitable to account for the short substorm onset time scale. Ref. [46] introduced an ion tearing mode with a growth rate γ_{ion} to be

$$\gamma_{ion} \approx \pi^{1/2}(u_i/L)(\rho_{ei}/L)^{3/2}, \tag{5}$$

assuming a long wavelength mode of $k_x^2 L^2 << 1$ and $T_i/T_e >> 1$. It is shown that even a small component of the magnetic field normal to the current sheet can stabilize this tearing instability by electron compressibility [47,48]. However, ref. [49] have presented arguments that for a multiscale magnetotail the instability electric field may penetrate to the electron magnetized region and destabilize the current sheet. This possibility remains to be evaluated.

3.3.2. Cross-Field Current Instability

The instability CCI consists of the modified two-stream instability and the ion Weibel instability. A simplified picture of these two modes was illustrated in [50]. Both of these instabilities lie on the same dispersion surface and are driven by a relative motion between ions and electrons perpendicular to the local magnetic field. Oblique whistler waves are excited. In the modified two-stream mode, excited waves propagate nearly perpendicular to the magnetic field while the waves in the ion Weibel mode propagate close to the magnetic field. For a configuration where the magnetic field $\boldsymbol{B} = B\hat{e}_z$, and wave propagation is in the YZ plane at an angle θ from the z-axis, i.e., $\boldsymbol{k} = k_x\hat{e}_x + k_y\hat{e}_y = k\cos\theta$, together with cold plasma and electrostatic limit assumptions, the dispersion relation equation is found to be

$$\frac{\omega_{pe}^2 \cos^2\theta}{\omega^2} + \frac{\omega_{pi}^2}{(\omega - kV_o\sin\theta)^2} = 1 + \frac{\omega_{pe}^2 \sin^2\theta}{\Omega_e^2}, \tag{6}$$

where ω, ω_{pe}, ω_{pi}, and Ω_e are wave frequency, electron plasma frequency, ion plasma frequency, and electron gyrofrequency, respectively, and V_o is the ion drift relative to the electrons. For a small angle $\theta \approx m_e/m_i$, with $\xi_i = (\omega - k_y V_o)/kv_i$, $\xi_e = \omega/kv_e$ (v_i and v_e are the ion and electron thermal speeds), the real frequency ω_r and growth rate γ of the excited wave are

$$\omega_r \approx -\frac{k^2 c^2 \cos^2\theta}{\omega_{pe}^2} \text{ and } \gamma/\omega_r \approx \sqrt{\pi}\sin^2\theta\left[\xi_i/\beta_i + 0.5\xi_e\beta_e \exp\left(-\xi_e^2\right)\right]. \tag{7}$$

For a hot plasma with electron gyrorotation, the growth rate expression becomes rather complicated to a lengthy expression dependent on several parameters. The full expression of plasma dispersion relation equation is documented in [35].

3.4. Auroral Beads

Phenomena occurring near the substorm onset provide important clues for identifying the physical process for substorm onset. In particular, just before the auroral breakup at substorm onset, azimuthal structures develop along the breakup auroral arc during some tens of seconds beforehand. Such spatial structures, discovered from global auroral images by Viking UVI, were first reported by [51] and named as auroral beads (ABs). The ABs' brightness increases exponentially with the approach to the substorm onset time [52]. At present, more details on ABs are available and provide very stringent observational constraints for the physical process. Three mechanisms for ABs occurrence are proposed, namely plasma flow braking [15,53], near-Earth plasma instabilities such as cross-field current instability [54], and ballooning/interchange instability [55]. Another instability developed conceptually without rigorous theoretical treatment to show an appropriate dispersion relation equation is called the mating instability [56]. It starts with the assumption that the ABs are independent from the substorm onset process. This assumption is primarily based on the observation that auroral breakup can occur with substantial delay from the appearance of ABs. However, a counter argument to this reasoning is that the

auroral breakup occurs at the nonlinear stage of the instability, which is delayed by about three growth times of the instability. Since the instability growth rate depends on the in situ environment where the instability is excited, the delay can be quite variable, as shown in observations. The delay can be long if the growth rate is slow.

The combined properties of spatially periodic structures and their exponential growth of brightness naturally lead to the consideration of plasma instabilities (e.g., [4,51,57–78]). It is worth noting that TI is not suitable to account for azimuthal structures of ABs because it produces spatial structures mainly along the north–south direction rather than the azimuthal direction in the ionosphere.

There is a wide range for different wavelengths corresponding to different growth rates so that there is no "universal" wavelength, period, or growth rate for all ABs. The work in [74] (denoted hereafter as N16) provides a severe challenge in ABs studies in that there are three properties of ABs linked simultaneously, namely wavelength, growth rate, and period. A correct theory needs to show that these properties do match their values from observations.

Prior to the N16 publication, it was known that ABs' brightness has a distinct growth rate besides their wavelength. Ref. [53] expanded the plasma flow braking idea by postulating that ABs are caused by plasma flow braking at the stop layers where auroral streamers enter the dipolar region. This plasma flow braking model can account for the wavelength of the ABs well but has not yet predicted any exponential growth of their brightness.

The proposal of ballooning/interchange instability as the cause of ABs is based on PIC simulation [55]. This proposal would be strengthened if simultaneous wavelength, period, and growth rate inferred theoretically could be demonstrated to match with these parameters in ABs observations. However, since no theorical work is performed to derive the dispersion relation equation in [55], this task becomes unrealizable. On the other hand, the dispersion relation equation for CCI has been formulated, and so it can be used to relate these three parameters for ABs in individual cases. This work is described below.

The starting point to solve the dispersion relation equation for CCI is to define the plasma parameters in the magnetospheric site linking the ABs. Since these plasma parameters are unknown, it is necessary to explore what they are together with the downstream distance for the excited site. This is performed through trial and error in solving the CCI dispersion relation equation [54]. The ranges of parameters used are 0.1–3 cm^{-3} for number density N, 5–40 nT for magnetic field B, 0.1–10 keV for ion temperature T_i, 0.05–5 keV for electron temperature T_e, and 0.01–1 u_e for the relative drift V_d between ion and electron populations, where u_e is the electron thermal speed. The amplification factor A linking the ionospheric scale to the magnetospheric scale ranges from ~11 to ~33 by $A = 14 + (33 - 14)(r/6 - 1)$, where r is the downstream distance. The solution obtained from this procedure, however, does not guarantee a unique set of plasma parameters.

Figure 7 shows the parameters used to reproduce the characteristics of westward propagating ABs (WABs) with the parameter set $N = 1$ cm^{-3}, $B = 10$ nT, $T_i = 9$ keV, $T_i/T_e = 7$, and $V_d = 0.036$ $V_d \sim 2.6$ V_A, where V_A is the local Alfvén speed. The median values given in N16 are 98.7 $\pm$ 28.7 km for ionospheric wavelength, 0.04 $\pm$ 0.03/s for growth rate, and 18 $\pm$ 6 s for period. The shaded region in Figure 7a denotes the upper and lower limits (based on median $\pm$ quarters) of the ionospheric wavenumber in N16 (0.045–0.083 /km). Three solutions with the CD site at downstream distances of 10, 11, and 12 R_E are shown. All solutions have peaks within the observed range with only a slight difference between them. The observed median value of 0.064/km matches extremely well with the peak of the red curve for 11 R_E. The shaded region in Figure 7b denotes the upper and lower limits (again based on median $\pm$ quarters) of the period in N16 (12–24). The three solutions shown reproduce the associated periods quite well with the red curve for 11 R_E fitting the best within the observed ranges of period and wavenumber. The combined results indicate that CCI reproduces simultaneously the growth rate, the wavenumber, and period well within the observed limits for WABs with excitation near 11 R_E.

$$N = 1 \text{ cm}^{-3}, \, B = 10 \text{ nT}, \, T_i = 9 \text{ keV}, \, T_i/T_e = 7, \, V_d \sim 2.6 \, V_A$$
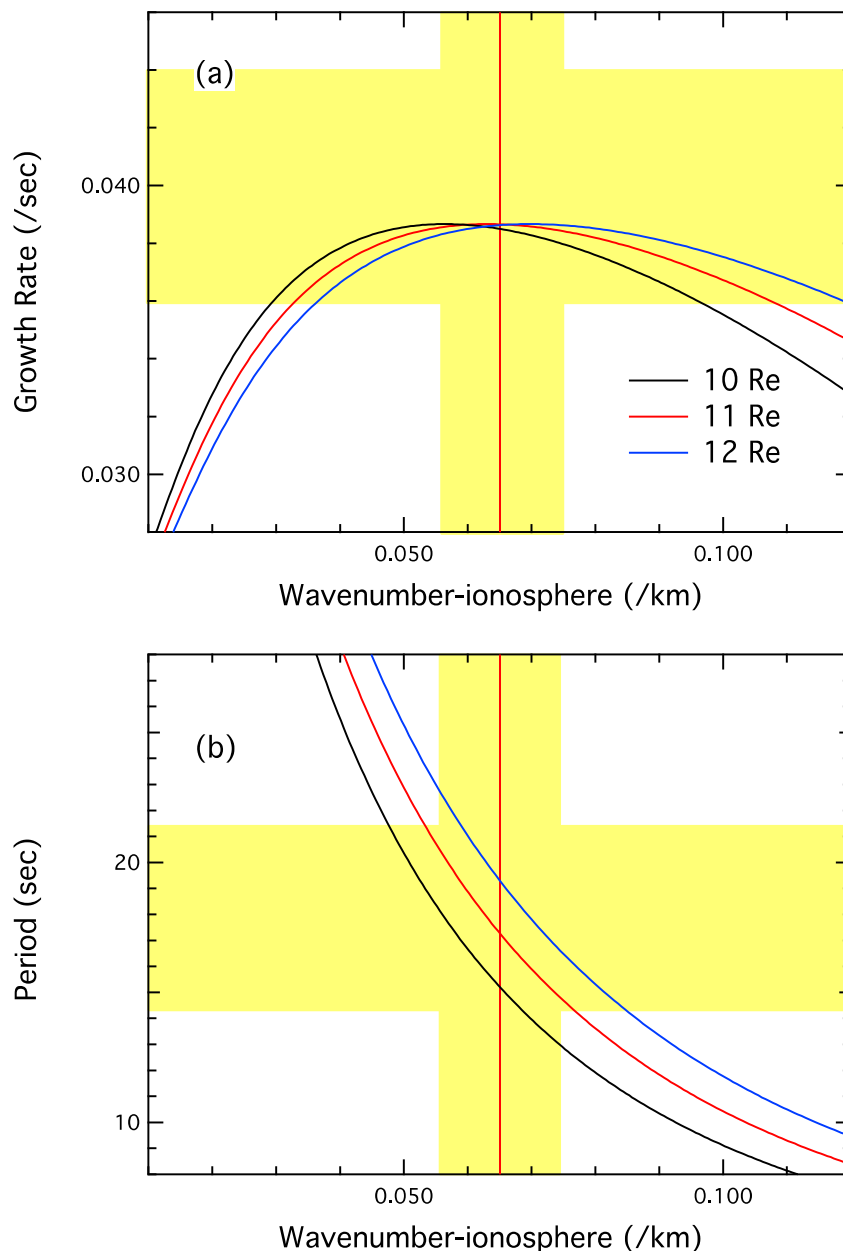
Figure 7. Comparison of observed (**a**) growth rate and (**b**) period as a function of ionospheric wavenumber for WABs with CCI predictions. The comparison shows that the WABs characteristics can be produced best by excitation of CCI at 11 R_E for the local plasma parameters as shown.

Simplified pictures of dynamo/load sites and field-aligned currents (FACs) generation from CD can be visualized in the following. The CCI disturbance generates a condition showing opposite signs of $J_\perp$ and ∇B on the west and east sides of the CD. From Equation (2), opposite signs of FACs are produced. This is shown in more detail in Figure 8. The meridian view (a) shows that CD causes dipolarization and magnetic field lines to collapse Earthward. The electrons tend to tie to the magnetic field lines due to their gyromotion and move Earthward while the ions lag behind. Even with a partial slippage of magnetic field line from the electrons, the differential motions of ions and electrons will create a net positive charge at the tailward end of the CD site and a net negative charge at the Earthward end, leading to an Earthward-directed electric field and $J \bullet E < 0$, i.e., a dynamo created by the CD site. Electrons at the Earthward side move down along the mag-

netic field line to reduce the net negative charge and generate an upward FAC. Similarly, electrons from the ionosphere move upward along the magnetic field line to reduce the net positive charge at the tailward end of the CD site. This in turn produces a downward FAC as shown. These FACs close in the ionosphere to produce an equatorward current. The magnetospheric electric field is transmitted to the ionosphere by the magnetic field lines and produces an equatorward electric field, leading to $J \bullet E > 0$, i.e., a load powered by the dynamo in the CD site.

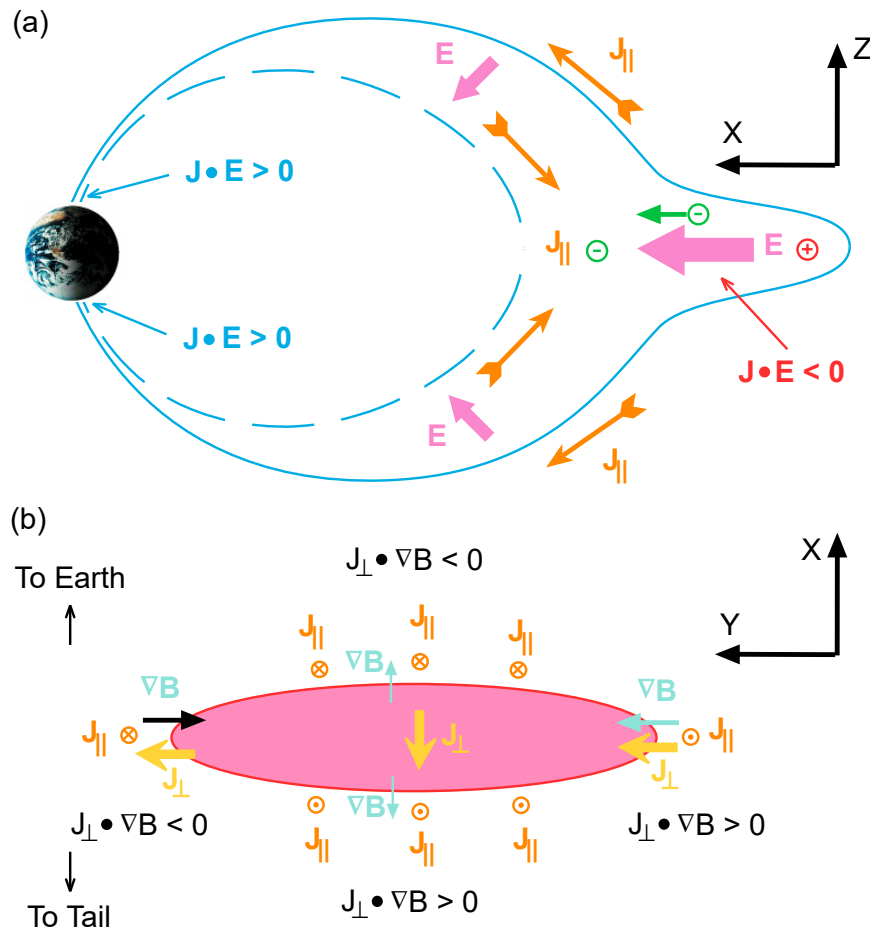**Figure 8.** The CCI disturbance generates a condition showing opposite signs of $J_\perp$ and ∇B on the west and east sides of the CD (**a**), and based on Equation (2), opposite signs of FACs are produced to produce the periodic bead structure in the ionosphere (**b**).

Figure 8b shows an equatorial cut of the CD site. Dipolarization creates an Earthward-directed magnetic field gradient at the Earthward side of the CD site ($J_\perp \bullet \nabla B < 0$) and a slightly rarefied magnetic field region at the tailward side, giving a tailward-directed magnetic field gradient ($J_\perp \bullet \nabla B > 0$). The current $J_\perp$ here refers to the radial component of the current in the plasma sheet. For the dawn–dusk direction, the current $J_\perp$ here denotes the cross-tail component of the current in the plasma sheet. The product $J_\perp \bullet \nabla B > 0$ occurs on the dawn side of CD, generating a downward FAC based on Equation (2). On the dusk side of CD, $J_\perp \bullet \nabla B < 0$ to produce an upward FAC.

The link between ABs formation and CD is described in more details in Figure 9. The appearance of the conjugacy of ABs in Figure 9a provides compelling evidence for the mechanism to be at the equatorial plane [76]. Since the ABs are not located at the poleward edge of the auroral oval where the magnetic field lines are mapped to an MR site in the magnetotail, this valuable clue indicates that the onset process resides well within the plasma sheet. In other words, the auroral substorm onset site is not directly mapped to an MR site where the open magnetic field lines become closed ones. The ABs site in the

magnetosphere likely maps along magnetic field lines to the magnetic transition region where the magnetic field configuration changes from dipolar to tail-like ([78] at ~5–15 R_E downtail). Figure 9b shows the link between each ripple produced by CD in the magnetotail and the ABs in the ionosphere. Figure 9c further indicates that these CD ripples can be the result of current filamentation and field-aligned electron acceleration by CCI using PIC simulation as described in [35].
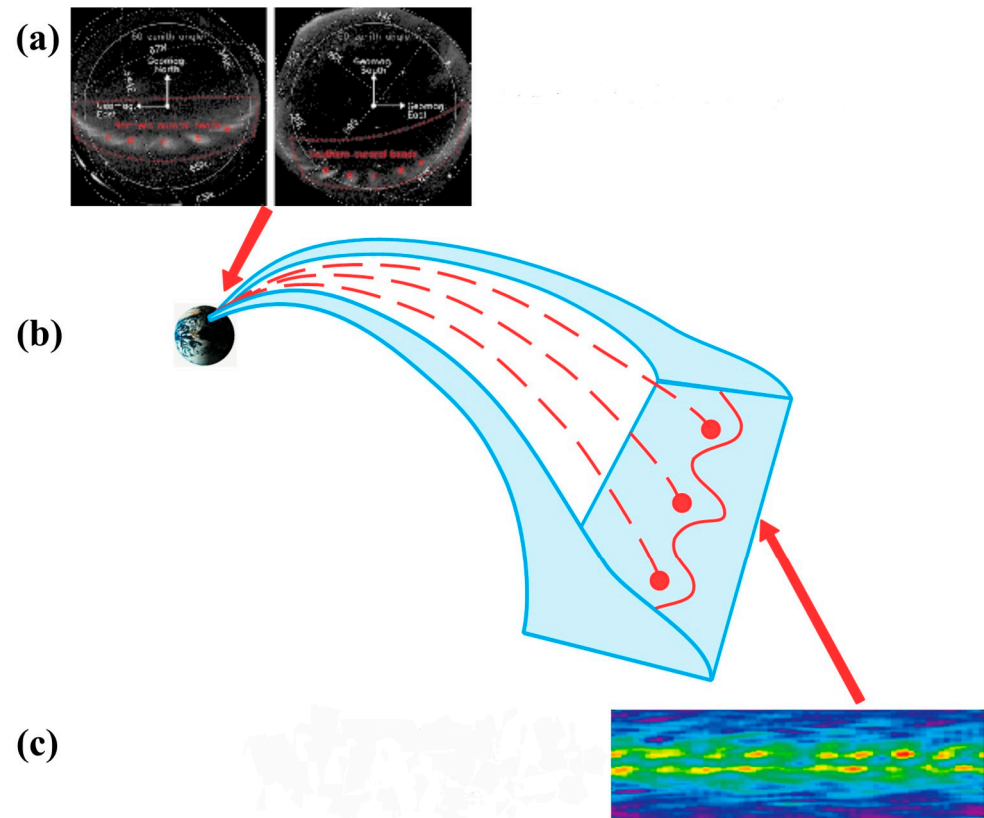

Figure 9. (**a**) A schematic diagram to show the conjugacy of auroral beads by ground-based observations from both northern and southern hemispheres, (**b**) the wavelengths in the magnetospheric equatorial plane corresponding to the periodic structure of the auroral beads, and (**c**) the current filamentation and electron acceleration arising from CCI excitation.

4. Conclusions

Dualism exists in magnetospheric research similar to the dualism in the treatment of electromagnetic waves with either Maxwell's equation in a continuum medium or quantized as individual photons. For space plasma, it can be treated as a continuum or as a collection of individual particles. Due to this dualism, one can use magnetic field ***B*** and plasma flow ***u*** in a continuum medium as primary parameters in the ***Bu*** paradigm or by adopting electric field ***E*** and electrical current ***j*** in a collection of individual particles as primary parameters in the ***Ej*** paradigm. Each paradigm has its merits and limitations. Which paradigm is better is highly dependent on the magnetospheric phenomenon under investigation. No one paradigm is perfect. There is no guarantee that large-scale plasma dynamics can always be treated accurately by the ***Bu*** paradigm. Insisting on only one paradigm being superior to the other for treating all magnetospheric problems would be inappropriate and stifle innovative thinking in scientific pursuits.

Since there is a prevalent adoption of the ***Bu*** paradigm, this article aims to demonstrate that there are merits in treating magnetospheric phenomena with the ***Ej*** paradigm. With this goal, several aspects of magnetospheric dynamics are discussed with emphasis on the ***Ej*** paradigm. The advantages of this viewpoint are illustrated in the topic of magnetic flux transport during substorm dipolarization. It is shown why the ***Bu*** paradigm can be

inappropriate in treating some cases of magnetic flux transport due to the violation of the frozen-in condition, a necessary condition for the application of the ***Bu*** paradigm. The disturbance generated by current disruption is found to lie outside the realm of the ***Bu*** paradigm description due to its fast temporal variation and short spatial structures. In reviewing the research based on the ***Ej*** paradigm cohesively, several significant features emerge that have not been recognized previously. In particular, in one detailed case study, the associated power dissipation in current disruption is found to be about one order of magnitude higher than that in the electron diffusion region for magnetic reconnection. The roles of tearing instability and cross-field current instability in understanding magnetotail phenomena are also examined. It is concluded that the former instability is not compatible with auroral beads formed in pre-substorm-onset auroral arcs. On the other hand, the latter instability can predict the wavelength, growth rate, and period simultaneously with a suitable choice of magnetotail parameters. The recently proposed mating instability does not provide a means to predict these parameters for comparison with observations, which is also new from the cohesive evaluation of the ***Ej*** paradigm. Overall, adopting electric field and electric current as the primary quantities in dynamic evolution provides a viable and insightful way to view magnetospheric phenomena besides using magnetic field and plasma flow as the primary dynamic drivers.

Institutional Review Board Statement: The Institutional Review was made by the Group Supervisor without an approval number.

Informed Consent Statement: Not applicable.

Data Availability Statement: Support data are available in public data facilities: NASA CDAweb.

Conflicts of Interest: The author declares no conflict of interest.

References

1. Lui, A.T.Y. *Electric Current Approach to Magnetospheric Dynamics and the Distinction between Current Disruption And Magnetic Reconnection, Magnetospheric Current Systems*; Ohtani, S., Fujii, R., Hesse, M., Lysak, R.L., Eds.; AGU Monograph; AGU: Washington, DC, USA, 2000; Volume 118, pp. 31–40.
2. Alfvén, H. Electrical currents in cosmic plasmas. *Rev. Geophys.* **1977**, *15*, 271. [CrossRef]
3. Yoon, P.H.; Lui, A.T.Y. Nonlinear analysis of generalized cross-field current instability. *Phys. Fluids B* **1993**, *5*, 836–853. [CrossRef]
4. Yoon, P.H.; Lui, A.T.Y.; Chang, C. Lower-hybrid-drift instability operative in the geomagnetic tail. *Phys. Plasmas* **1994**, *1*, 3033–3043. [CrossRef]
5. Lui, A.T.Y. Current disruption in the Earth's magnetosphere: Observations and models. *J. Geophys. Res.* **1996**, *101*, 13067–13088. [CrossRef]
6. Akasofu, S.-I. Electric current approach studying both auroral substorms and solar flares together. *Front. Astron. Space Sci.* **2020**, *7*, 4. [CrossRef]
7. Vasyliunas, V.M. Time scale for magnetic field changes after sub-storm onset: Constraints from dimensional analysis. In *Physics of Space Plasmas*; Chang, T., Jasperse, J.R., Eds.; MIT Center for Geo/Cosmo Plasma Physics: Cambridge, MA, USA, 1996; pp. 553–560.
8. Vasyliunas, V.M. Time evolution of electric fields and currentsand the generalized Ohm's law. *Ann. Geophys.* **2005**, *23*, 1347–1354. [CrossRef]
9. Parker, E.N. *Tutorial: Newton, Maxwell, and Magnetospheric Physics, Magnetospheric Current Systems*; Ohtani, S., Fujii, R., Hesse, M., Lysak, R.L., Eds.; AGU Monograph 2000; AGU: Washington, DC, USA, 2000; Volume 118, pp. 1–10.
10. Lui, A.T.Y.; Chapman, S.C.; Liou, K.; Newell, P.T.; Meng, C.-I.; Brittnacher, M.; Parks, G.K. Is the dynamic magnetosphere an avalanching system? *Geophys. Res. Lett.* **2000**, *27*, 911–914. [CrossRef]
11. Lui, A.T.Y. Time development of electric fields and currents in space plasmas. *Ann. Geophys.* **2006**, *24*, 1137–1143. [CrossRef]
12. Lui, A.T.Y. Reduction of the cross-tail current during near-Earth dipolarization with multi-satellite observations. *J. Geophys. Res.* **2011**, *116*, A12239. [CrossRef]
13. Sato, T.; Iijima, T. Primary sources of large-scale Birkeland currents. *Space Sci. Rev.* **1979**, *24*, 347. [CrossRef]
14. Hasegawa, A.; Sato, T. *Generation of Field Aligned Current during Substorm, Dynamics of the Magnetosphere*; Springer: Dordrecht, The Netherlands, 1979.
15. Haerendel, G. Field-aligned currents in the Earth's magnetosphere. *Geophys. Monogr. Ser.* **1990**, *58*, 539.

16. Akasofu, S.I. *Polar and Magnetosphere Substorms*; Astrophysics & Space Science Library: Dordrecht, The Netherlands, 1968; Volume 11, ISBN 90-277-0108-3.
17. Rostoker, G.; Akasofu, S.-I.; Foster, J.; Greenwald, R.; Kamide, Y.; Kawasaki, K.; Lui, A.; McPherron, R.; Russell, C. Magnetospheric substorms-definition and signatures. *J. Geophys. Res.* **1980**, *85*, 1663–1668. [CrossRef]
18. Nakamura, R.; Baumjohann, W.; Klecker, B.; Bogdanova, Y.; Balogh, A.; Rème, H.; Bosqued, J.M.; Dandouras, I.; Sauvaud, J.A.; Glassmeier, K.-H.; et al. Motion of the dipolarization front during a flow burst event observed by Cluster. *Geophys. Res. Lett.* **2002**, *29*, 1942. [CrossRef]
19. Runov, A.; Angelopoulos, V.; Sitnov, M.I.; Sergeev, V.A.; Bonnell, J.; McFadden, J.P.; Larson, D.; Glassmeier, K.-H.; Auster, U. THEMIS observations of an earthward-propagating dipolarization front. *Geophys. Res. Lett.* **2009**, *36*, L14106. [CrossRef]
20. Sergeev, V.; Angelopoulos, V.; Apatenkov, S.; Bonnell, J.; Ergun, R.; Nakamura, R.; McFadden, J.; Larson, D.; Runov, A. Kinetic structure of the sharp injection/dipolarization front in the flow-braking region. *Geophys. Res. Lett.* **2009**, *36*, L21105. [CrossRef]
21. Zhou, X.-Z.; Angelopoulos, V.; Sergeev, V.; Runov, A. Accelerated ions ahead of earthward propagating dipolarization fronts. *J. Geophys. Res.* **2010**, *115*, A00I03. [CrossRef]
22. Zhang, X.-J.; Angelopoulos, V.; Runov, A.; Zhou, X.-Z.; Bonnell, J.; McFadden, J.P.; Larson, D.; Auster, U. Current carriers near dipolarization fronts in the magnetotail: A THEMIS event study. *J. Geophys. Res.* **2011**, *116*, A00I20. [CrossRef]
23. Fu, H.S.; Khotyaintsev, Y.V.; André, M.; Vaivads, A. Fermi and betatron acceleration of suprathermal electrons behind dipolarization fronts. *Geophys. Res. Lett.* **2011**, *38*, L16104. [CrossRef]
24. Lyons, L.R.; Nishimura, Y.; Xing, X.; Runov, A.; Angelopoulos, V.; Donovan, E.; Kikuchi, T. Coupling of dipolarization front flow bursts to substorm expansion phase phenomena within the magnetosphere and ionosphere. *J. Geophys. Res.* **2012**, *117*, A02212. [CrossRef]
25. Huang, S.Y.; Zhou, M.; Deng, X.H.; Yuan, Z.G.; Pang, Y.; Wei, Q.; Su, W.; Li, H.M.; Wang, Q.Q. Kinetic structure and wave properties associated with sharp dipolarization front observed by Cluster. *Ann. Geophys.* **2012**, *30*, 97–107. [CrossRef]
26. Hwang, K.; Goldstein, M.L.; Moore, T.E.; Walsh, B.M.; Baishev, D.G.; Moiseyev, A.V.; Shevtsov, B.M.; Yumoto, K. Atailward moving current sheet normal magnetic field front followed by an earthward moving dipolarization front. *J. Geophys. Res. Space Physics.* **2014**, *119*, 5316–5327. [CrossRef]
27. Liu, J.; Angelopoulos, V.; Runov, A.; Zhou, X.-Z. On the current sheets surrounding dipolarizing flux bundles in the magnetotail: The case for wedgelets. *J. Geophy. Res. Space Physics.* **2013**, *118*, 2000–2020. [CrossRef]
28. Liu, J.; Angelopoulos, V.; Zhou, X.-Z.; Runov, A. Magnetic flux transport by dipolarizing flux bundles. *J. Geophy. Res. Space Physics.* **2014**, *119*, 909–926. [CrossRef]
29. Runov, A.; Angelopoulos, V.; Zhou, X.-Z.; Zhang, X.-J.; Li, S.; Plaschke, F.; Bonnell, J. A THEMIS multicase study of dipolarization fronts in the magnetotail plasma sheet. *J. Geophys. Res.* **2011**, *116*, A05216. [CrossRef]
30. Lui, A.T.Y. Dipolarization fronts and magnetic flux transport. *Geosci. Lett.* **2015**, *2*, 15. [CrossRef]
31. Angelopoulos, V.; Kennel, C.F.; Coroniti, F.V.; Pellat, R.; Kivelson, M.G.; Walker, R.J.; Russell, C.T.; Baumjohann, W.; Feldman, W.C.; Gosling, J.T. Statistical characteristics of bursty bulk flow events. *J. Geophys. Res.* **1994**, *99*, 21257–21280. [CrossRef]
32. Yao, Z.H.; Liu, J.; Owen, C.J.; Forsyth, C.; Rae, I.J.; Pu, Z.Y.; Fu, H.S.; Zhou, X.-Z.; Shi, Q.Q.; Du, A.M.; et al. A physical explanation for the magnetic decrease ahead of dipolarization fronts. *Ann. Geophys.* **2015**, *33*, 1301–1309. [CrossRef]
33. Takahashi, K.; Zanetti, L.J.; Lopez, R.E.; McEntire, R.W.; Potemra, T.A.; Yumoto, K. Disruption of the magnetotail current sheet observed by AMPTE/CCE. *Geophys. Res. Lett.* **1987**, *14*, 1019–1022. [CrossRef]
34. Lui, A.T.Y. Cross-tail current evolution during substorm depolarization. *Ann. Geophys.* **2013**, *31*, 1131–1142. [CrossRef]
35. Lui, A.T.Y. Potential plasma instabilities for substorm expansion onset. *Space Sci. Rev.* **2004**, *113*, 127–206. [CrossRef]
36. Pritchett, P.L.; Coroniti, F.V. Structure and consequences of the kinetic ballooning/interchange instability in the magnetotail. *J. Geophys. Res. Space Physics.* **2013**, *118*, 146–159. [CrossRef]
37. Torbert, R.B.; Burch, J.L.; Phan, T.D.; Hesse, M.; Argall, M.R.; Shuster, J.; Ergun, R.E.; Alm, L.; Nakamura, R.; Genestreti, K.J.; et al. Electron-scale dynamics of the diffusion region during symmetric magnetic reconnection in space. *Science* **2018**, *362*, 1391–1395. [CrossRef]
38. Lui, A.T.Y.; Consolini, G. *Substorm Disturbance Propagation from a Two-Dimensional Cellular Automaton Model, Multiscale Coupling of Sun-Earth Processes*; Lui, A.T.Y., Kamide, Y., Consolini, G., Eds.; Elsevier: Amsterdam, The Netherlands, 2005; pp. 357–364.
39. Consolini, G.; Kretzschmar, M.; Lui, A.T.Y.; Zimbardo, G.; Macek, W.M. On the magnetic field fluctuations during magnetospheric tail current disruption: A statistical approach. *J. Geophys. Res.* **2005**, *110*, A07202. [CrossRef]
40. Zelenyi, L.M.; Delcourt, D.C.; Malova, H.V.; Sharma, A.S. "Aging" of the magnetotail thin current sheets. *Geophys. Res. Lett.* **2002**, *29*, 49-1–49-4. [CrossRef]
41. Zelenyi, L.M.; Malova, H.V.; Popov, V.Y.; Delcourt, D.; Sharma, A.S. Nonlinear equilibrium structure of thin currents sheets: Influence of electron pressure anisotropy. *Nonlinear Process. Geophys.* **2004**, *11*, 579–587. [CrossRef]
42. Grigorenko, E.E.; Zelenyi, L.M.; DiBraccio, G.; Ermakov, V.N.; Shuvalov, S.D.; Malova, H.V.; Poppov, V.Y.; Halekas, J.S.; Mitchell, D.J.; Dubinin, E. Thin current sheets of sub-ion scales observed by MAVEN in the Martian magnetotail. *Geophys. Res. Lett.* **2019**, *46*, 6214–6222. [CrossRef]
43. Büchner, J.; Zelenyi, L.M. Regular and chaotic charged particle motion in magnetotail like field reversals: 1. Basic theory of trapped motion. *J. Geophys. Res.* **1989**, *94*, 11821–11842. [CrossRef]

44. Zelenyi, L.M.; Malova, H.V.; Leonenko, M.V.; Grigorenko, E.E.; Popov, V.Y. Equilibrium configurations of super-thin current sheets in space plasma: Characteristic scaling of multilayer structures. *J. Geophys. Res. Space Phys.* **2022**, *127*, e2022JA030881. [CrossRef]
45. Coppi, B.; Laval, G.; Pellat, R. Dynamics of the geomagnetic tail. *Phys. Rev. Lett.* **1966**, *16*, 1207–1210. [CrossRef]
46. Schindler, K. A theory of the substorm mechanism. *J. Geophys. Res.* **1974**, *79*, 2803–2810. [CrossRef]
47. Pellat, R.; Coroniti, F.V.; Pritchett, P.L. Does ion tearing exist? *Geophys. Res. Lett.* **1991**, *18*, 143–146. [CrossRef]
48. Brittnacher, M.; Quest, K.B.; Karimabadi, H. A study of the effect of pitch angle and spatial diffusion on tearing instability using a new finite element based linear code. *J. Geophys. Res.* **1998**, *103*, 4587–4596. [CrossRef]
49. Sitnov, M.I.; Schindler, K. Tearing stability of a multiscale magnetotail current sheet. *Geophys. Res. Lett.* **2010**, *37*, 8. [CrossRef]
50. Lui, A.T.Y.; Chang, C.-L.; Mankofsky, A.; Wong, H.-K.; Winske, D. A cross-field current instability for substorm expansions. *J. Geophys. Res.* **1991**, *96*, 11389–11401. [CrossRef]
51. Henderson, M.G. *Implications of Viking Imager Results for Substorm Models*; University of Calgary: Calgary, AB, Canada, 1994.
52. Donovan, E.; Liu, W.; Liang, J.; Spanswick, E.; Voronkov, I.; Connors, M.; Syrjäsuo, M.; Baker, G.; Jackel, B.; Trondsen, T.; et al. Simultaneous THEMIS in situ and auroral observations of a small substorm. *Geophys. Res. Lett.* **2008**, *35*, L17S18. [CrossRef]
53. Haerendel, G. Substorm onset: Current sheet avalanche and stop layer. *J. Geophys. Res. Space Phys.* **2015**, *120*, 1697–1714. [CrossRef]
54. Lui, A.T.Y. Evaluation of the cross-field current instability as a substorm onset process with auroral bead properties. *J. Geophys. Res. Space Phys.* **2020**, *123*, e2020JA027867. [CrossRef]
55. Pritchett, P.L.; Coroniti, F.V.; Nishimura, Y. The kinetic ballooning/interchange instability as a source of dipolarization fronts and auroral streamers. *J. Geophys. Res. Space Phys.* **2014**, *119*, 4723–4739. [CrossRef]
56. Haerendel, G.; Frey, H. The onset of a substorm and the mating instability. *J. Geophys. Res. Space Phys.* **2021**, *126*, e2021JA029492. [CrossRef]
57. Samson, J.C.; Wallis, D.D.; Hughes, T.J.; Creutzberg, F.; Ruohoniemi, J.M.; Greewalkd, R.A. Substorm intensifications and field line resonances in the nightside magnetosphere. *J. Geophys. Res.* **1992**, *97*, 8495–8518. [CrossRef]
58. Yoon, P.H.; Lui, A.T.Y.; Sitnov, M. Generalized lower-hybrid drift instabilities in current-sheet equilibrium. *Phys. Plasmas* **2002**, *9*, 1526–1538. [CrossRef]
59. Pu, Z.Y.; Korth, A.; Chen, Z.X.; Friedel RH, W.; Zong, Q.G.; Wang, X.M.; Wong, M.H.; Fu, S.Y.; Pulkkinen, T.I. MHD drift ballooning instability near the inner edge of the near-Earth plasma sheet. *J. Geophys. Res.* **1997**, *102*, 14397–14406. [CrossRef]
60. Voronkov, I.; Rankin, R.; Frycz, P.; Tikhonchuk, V.T.; Samson, J.C. Coupling of shear flow and pressure gradient instabilities. *J. Geophys. Res.* **1997**, *102*, 9639–9650. [CrossRef]
61. Cheng, C.Z.; Lui, A.T.Y. Kinetic ballooning instability for substorm onset and current disruption observed by AMPTE/CCE. *Geophys. Res. Lett.* **1998**, *25*, 4091–4094. [CrossRef]
62. Friedrich, E.; Samson, J.C.; Voronkov, I.; Rostoker, G. Dynamics of the substorm expansive phase. *J. Geophys. Res.* **2001**, *106*, 13145–13163. [CrossRef]
63. Cheng, C.Z. Physics of substorm growth phase, onset, and depolarization. *Space Sci. Rev.* **2004**, *113*, 207–270. [CrossRef]
64. Samson., J.C.; Dobias, P. Explosive instabilities and substorm intensifications in the Earth's magnetotail. In *Multiscale Coupling of Sun-Earth Processes*; Lui, A.T.Y., Kamide, Y., Consolini, G., Eds.; Elsevier B. V.: Amsterdam, The Netherlands, 2005; pp. 235–251.
65. Saito, M.H.; Miyashita, Y.; Fujimoto, M.; Shinohara, I.; Saito, Y.; Liou, K.; Mukai, T. Ballooning mode waves prior to substorm-associated dipolarizations: Geotail observations. *Geophys. Res. Lett.* **2008**, *35*, L07103. [CrossRef]
66. Liang, J.; Donovan, E.F.; Liu, W.W.; Jackel, B.; Syrjasuo, M.; Mende, S.B.; Frey, H.U.; Angelopoulos, V.; Connors, M. Intensification of pre-existing auroral arc at substorm expansion phase onset: Wave-like disruption during the first tens of seconds. *Geophys. Res. Lett.* **2008**, *35*, L17S19. [CrossRef]
67. Rae, I.J.; Mann, I.R.; Angelopoulos, V.; Murphy, K.R.; Milling, D.K.; Kale, A.; Frey, H.; Rostoker, G.; Russell, C.T.; Watt, C.; et al. Near-Earth initiation of a terrestrial substorm. *J. Geophys. Res.* **2009**, *114*, A07220. [CrossRef]
68. Rae, I.J.; Watt CE, J.; Mann, I.R.; Murphy, K.R.; Samson, J.C.; Kabin, K.; Angelopoulos, V. Optical characterization of the growth and spatial structure of a substorm onset arc. *J. Geophys. Res.* **2010**, *115*, A10222. [CrossRef]
69. Keiling, A. Pi2 pulsations driven by ballooning instability. *J. Geophys. Res.* **2012**, *117*. [CrossRef]
70. Liu, W.W.; Liang, J.; Donovan, E.F.; Spanswick, E. If substorm onset triggers tail reconnection, what triggers substorm onset? *J. Geophys. Res.* **2012**, *117*, A11220. [CrossRef]
71. Kozelova, T.V.; Kozelov, B.V. Substorm-associated explosive magnetic field stretching near the earthward edge of the plasma sheet. *J. Geophys. Res. Space Phys.* **2013**, *118*, 3323–3335. [CrossRef]
72. Xing, X.; Liang, J.; Spanswick, E.; Lyons, L.; Angelopoulos, V. Auroral wave structures and ballooning instabilities in the plasma sheet. *J. Geophys. Res. Space Phys.* **2013**, *118*, 6319–6326. [CrossRef]
73. Kalmoni, N.M.E.; Rae, I.J.; Watt, C.E.J.; Murphy, K.R.; Forsyth, C.; Owen, C.J. Statistical characterization of the growth and spatial scales of the sub storm onset arc. *J. Geophys. Res. Space Phys.* **2015**, *120*, 8503–8516. [CrossRef]
74. Nishimura, Y.; Yang, J.; Pritchett, P.L.; Coroniti, F.V.; Donovan, E.F.; Lyons, L.R.; Wolf, R.A.; Angelopoulos, V.; Mende, S.B. Statisitcal properties of substorm auroral onset beads/rays. *J. Geophys. Res. Space Phys.* **2016**, *121*, 8661–8676. [CrossRef]
75. Lui, A.T.Y. Dipolarization front and current disruption. *Geophys. Res. Lett.* **2016**, *43*, 10050. [CrossRef]

76. Motoba, T.; Hosokawa, K.; Kodokura, A.; Sato, N. Magnetic conjugacy of northern and southern auroral beads. *Geophys. Res. Lett.* **2012**, *39*, L08108. [CrossRef]

77. Lui, A.T.Y. Cross-field current instability for auroral bead formation in breakup arcs. *Geophys. Res. Lett.* **2016**, *43*, 6087–6095. [CrossRef]

78. Lui, A.T.Y.; Burrows, J.R. On the location of auroral arcs near substorm onset. *J. Geophys. Res.* **1978**, *83*, 3342–3348. [CrossRef]